Effect of collisional elasticity on the Bagnold rheology of sheared frictionless two-dimensional disks

Daniel Vågberg,[1] Peter Olsson,[2] and S. Teitel[3]
[1]*Laboratoire Charles Coulomb, UMR 5221 CNRS, Université Montpellier, Montpellier, France*
[2]*Department of Physics, Umeå University, 901 87 Umeå, Sweden*
[3]*Department of Physics and Astronomy, University of Rochester, Rochester, New York 14627, USA*
(Received 28 September 2016; revised manuscript received 29 December 2016; published 30 January 2017)

We carry out constant volume simulations of steady-state, shear-driven flow in a simple model of athermal, bidisperse, soft-core, frictionless disks in two dimensions, using a dissipation law that gives rise to Bagnoldian rheology. Focusing on the small strain rate limit, we map out the rheological behavior as a function of particle packing fraction ϕ and a parameter Q that measures the elasticity of binary particle collisions. We find a $Q^*(\phi)$ that marks the clear crossover from a region characteristic of strongly inelastic collisions, $Q < Q^*$, to a region characteristic of weakly inelastic collisions, $Q > Q^*$, and give evidence that $Q^*(\phi)$ diverges as $\phi \to \phi_J$, the shear-driven jamming transition. We thus conclude that the jamming transition at any value of Q behaves the same as the strongly inelastic case, provided one is sufficiently close to ϕ_J. We further characterize the differing nature of collisions in the strongly inelastic vs weakly inelastic regions, and recast our results into the constitutive equation form commonly used in discussions of hard granular matter.

DOI: 10.1103/PhysRevE.95.012902

I. INTRODUCTION

In a system of athermal ($T = 0$) granular particles with soft- or hard-core contact interactions, as the particle packing fraction ϕ increases, the system will undergo a jamming transition from a liquidlike flowing state to a rigid but disordered solid state, at a critical packing fraction ϕ_J [1,2]. For particles without intergranular friction, this jamming transition is in general continuous and the transport coefficients characterizing the liquid state response to shear will, in the low strain rate limit $\dot\gamma \to 0$, diverge continuously as ϕ_J is approached from below [3–5].

For the case where the particle contact interaction is the spring-dashpot model [6], where energy dissipation is due only to particle collisions and is proportional to the difference in the components of the colliding particles' velocities normal to the surface at the point of contact, the system is known [7–14] to display Bagnoldian rheology [15] with pressure p, and shear stress σ, scaling with shear strain rate $\dot\gamma$ as $p,\sigma \propto \dot\gamma^2$, at sufficiently slow strain rates. In a recent work [5] we considered the shear-driven jamming transition for such a model of athermal, bidisperse, frictionless, soft-core disks in two dimensions. We applied a critical scaling analysis to determine the divergence of the Bagnold transport coefficients, $p/\dot\gamma^2$ and $\sigma/\dot\gamma^2$, as one asymptotically approaches ϕ_J from below. Our analysis was for the specific case of a system with strongly inelastic collisions.

In this work we systematically explore the effects on the system rheology when one varies the degree of collision elasticity away from the strongly inelastic limit. This question was previously considered by Otsuki, Hayakawa, and Luding (OHL) [16] who argued, from looking at simulations for several specific cases, that the critical scaling associated with the limit of strongly inelastic collisions always exists in a window of ϕ sufficiently close to the jamming ϕ_J, but that the width of this window decreases as the collisions become increasingly elastic, and ultimately vanishes in the limit of purely elastic collisions. They used this result to reconcile the behavior of transport coefficients observed in simulations of particles with strongly inelastic collisions, with earlier work on elastically (and nearly elastically) colliding particles [17–20]. However, they did not explicitly determine the location of this crossover from strongly inelastic to nearly elastic behavior, but only presented a schematic picture (their Fig. 18).

In the present work we reexamine this question by exploring rheological behavior over a wide range of packing fraction ϕ, and a parameter Q that controls the degree of elasticity of particle collisions. We focus our attention on the hard-core limit of our soft-core particle model, which is attained when the applied shear strain rate $\dot\gamma$ is sufficiently small and so particle overlaps become negligible. We find that as Q increases at fixed ϕ, there is a sharp, but nonsingular, crossover: at small Q there is a region of behavior characteristic of strongly inelastic collisions, in which transport coefficients are roughly independent of Q; at large Q there is a region of behavior characteristic of weakly inelastic collisions, where transport coefficients increase with increasing Q (see Fig. 1). We explicitly locate this crossover $Q^*(\phi)$ and provide evidence that it diverges as $\phi \to \phi_J$. Thus, a system at any fixed Q is always in the strongly inelastic region $Q < Q^*$ if one is sufficiently close to ϕ_J. This result thus supports the conclusions of OHL [16].

The remainder of our paper is organized as follows. In Sec. II we present our numerical model and dimensionless variables, describe the calculation of the different pieces of the pressure tensor and corresponding Bagnold transport coefficients, and give details of our numerical simulation method. In Sec. III we present our numerical results for the Bagnold coefficients, determine the crossover $Q^*(\phi)$, discuss the implications for the jamming transition as a function of Q, and discuss the effect of varying Q on the macroscopic friction $\mu = \sigma/p$. We also discuss the different behavior of the strongly inelastic vs the weakly inelastic region with regard to the impact angle and time scales of collisions, as well as the average particle contact number $\langle Z \rangle$. Finally, we recast our results into the form of the constitutive equations commonly used to discuss shear flow in systems of hard-core granular particles [21–25]. In Sec. IV we summarize our conclusions.

 ©2017 American Physical Society

II. MODEL AND SIMULATION METHOD

A. Model

We use a well-studied model [1] of frictionless, bidisperse, soft-core circular disks in two dimensions, with equal numbers of big and small particles with diameter ratio $d_b/d_s = 1.4$. Particles interact only when they come into contact, in which case they repel with an elastic potential,

$$\mathcal{V}_{ij}(r_{ij}) = \begin{cases} \frac{1}{\alpha}k_e(1 - r_{ij}/d_{ij})^\alpha, & r_{ij} < d_{ij} \\ 0, & r_{ij} \geqslant d_{ij}. \end{cases} \tag{1}$$

Here $r_{ij} \equiv |\mathbf{r}_{ij}|$, where $\mathbf{r}_{ij} \equiv \mathbf{r}_i - \mathbf{r}_j$ is the center to center displacement from particle j at position $\mathbf{r}_j$ to particle i at $\mathbf{r}_i$, and $d_{ij} \equiv (d_i + d_j)/2$ is the average of their diameters. In this work we will use the value $\alpha = 2$, corresponding to a harmonic repulsion. The resulting elastic force on particle i from particle j is,

$$\mathbf{f}_{ij}^{\rm el} = -\frac{d\mathcal{V}_{ij}(r_{ij})}{d\mathbf{r}_i} = \frac{k_e}{d_{ij}}\left(1 - \frac{r_{ij}}{d_{ij}}\right)^{\alpha-1}\hat{\mathbf{r}}_{ij}, \tag{2}$$

where $\hat{\mathbf{r}}_{ij} \equiv \mathbf{r}_{ij}/r_{ij}$ is the inward pointing normal direction at the surface of particle i.

Particles also experience a dissipative force when they come into contact. We take this force to be proportional to the projection of the velocity difference of the contacting particles onto the direction normal to the surface at the point of contact. The dissipative force on particle i from particle j is,

$$\mathbf{f}_{ij}^{\rm dis} = -k_d[(\mathbf{v}_i - \mathbf{v}_j)\cdot\hat{\mathbf{r}}_{ij}]\hat{\mathbf{r}}_{ij}, \tag{3}$$

where $\mathbf{v}_i \equiv d\mathbf{r}_i/dt$ is the center of mass velocity of particle i. We have earlier [14] denoted this model of dissipation as CD_n for normal contact dissipation. This dissipative force is well known to result in Bagnoldian rheology [7–14,21]. The combination of elastic and dissipative forces of Eqs. (2) and (3) is often referred to as the spring-dashpot model [6]. We note that the constants k_e and k_d, which define the strengths of our forces have different physical units.

Particle motion is governed by the deterministic Newton's equation,

$$m_i\frac{d^2\mathbf{r}_i}{dt^2} = \sum_j\left[\mathbf{f}_{ij}^{\rm el} + \mathbf{f}_{ij}^{\rm dis}\right], \tag{4}$$

where m_i is the mass of particle i and the sum is over all particles j in contact with particle i. In this work we take particles to have a mass proportional to their area, i.e., small particles have mass $m_s = \rho_0\pi(d_s/2)^2$ and big particles have mass $m_b = \rho_0\pi(d_b/2)^2$, with ρ_0 the mass per area. We define $m_0 = \frac{1}{2}\rho_0 d_s^2$ as a unit of mass [26].

The above microscopic dynamics possess two important time scales [14], the elastic and dissipative relaxation times,

$$\tau_e \equiv \sqrt{m_0 d_s^2/k_e}, \quad \tau_d \equiv m_0/k_d. \tag{5}$$

The parameter

$$Q \equiv \tau_d/\tau_e = \sqrt{m_0 k_e/(k_d d_s)^2} \tag{6}$$

measures the degree of elasticity of the collisions. For the harmonic interaction that we use, if we regarded the elastic potential of Eq. (1) as a spring, which did not break when particles lose contact, then $2\pi\tau_e$ would give the undamped natural period of oscillation, $2\tau_d$ would be the decay time, and Q would be the quality factor.

Q may also be related to the coefficient of restitution e of a collision. For the isolated head-on collision of two particles i and j, we have,

$$e = \exp\left[-\pi\Big/\sqrt{4\left(\frac{m_{ij}}{m_0}\right)\left(\frac{d_s}{d_{ij}}\right)^2 Q^2 - 1}\,\right], \tag{7}$$

where $m_{ij} = m_i m_j/(m_i + m_j)$ is the reduced mass of the two particles [6]. When $Q < (d_{ij}/2d_s)\sqrt{m_0/m_{ij}}$, so that the argument of the square root would be negative, the collision is completely inelastic with $e = 0$. For two small particles this happens when $Q < Q_d = 0.564$. Note, however, that in our two-dimensional geometry, a collision that is not strictly head-on will result in particles separating after the collision even if $e = 0$, since tangential relative motion is not dissipated by the force $\mathbf{f}_{ij}^{\rm dis}$ of Eq. (3).

Our system consists of a fixed total number particles N in a square box of fixed length L. L is chosen to set the particle packing fraction ϕ,

$$\phi = \frac{\pi N}{2L^2}\left[\left(\frac{d_s}{2}\right)^2 + \left(\frac{d_b}{2}\right)^2\right]. \tag{8}$$

To apply a uniform shear strain rate $\dot\gamma$ in the $\hat{\mathbf{x}}$ direction, we use periodic Lees-Edwards boundary conditions [27], so that a particle at position $\mathbf{r} = (r_x, r_y)$ has images at positions $(r_x + mL + n\gamma L, r_y + nL)$, with n, m integer and $\gamma = \dot\gamma t$ the total shear strain at time t.

B. Pressure tensor

To determine the global rheology of the system we measure the pressure tensor of each configuration. We can break this pressure tensor into three pieces [16,27]: the elastic part $\mathbf{p}^{\rm el}$, arising from the repulsive elastic forces of Eq. (2),

$$\mathbf{p}^{\rm el} \equiv \frac{1}{L^2}\sum_{i<j}\mathbf{f}_{ij}^{\rm el}\otimes\mathbf{r}_{ij}, \tag{9}$$

the dissipative part $\mathbf{p}^{\rm dis}$, arising from the dissipative forces of Eq. (3),

$$\mathbf{p}^{\rm dis} \equiv \frac{1}{L^2}\sum_{i<j}\mathbf{f}_{ij}^{\rm dis}\otimes\mathbf{r}_{ij}, \tag{10}$$

and the kinetic part $\mathbf{p}^{\rm kin}$ (sometimes called the streaming part),

$$\mathbf{p}^{\rm kin} \equiv \frac{1}{L^2}\sum_i m_i\delta\mathbf{v}_i\otimes\delta\mathbf{v}_i, \tag{11}$$

where $\delta\mathbf{v}_i \equiv \mathbf{v}_i - \dot\gamma y_i\hat{\mathbf{x}}$ is the fluctuation away from the linear average velocity profile that characterizes the uniform shear strain flow. The total pressure tensor is then,

$$\mathbf{p} = \mathbf{p}^{\rm el} + \mathbf{p}^{\rm dis} + \mathbf{p}^{\rm kin}. \tag{12}$$

The average pressure p and shear stress σ in the system are then,

$$p = \tfrac{1}{2}[\langle p_{xx}\rangle + \langle p_{yy}\rangle], \quad \sigma = -\langle p_{xy}\rangle, \tag{13}$$

where $\langle \dots \rangle$ represents an ensemble average over configurations in the sheared steady state. Also of potential interest is the pressure anisotropy δp and the deviatoric stress $\sigma_{\rm dev}$,

$$\delta p = \tfrac{1}{2}[\langle p_{xx}\rangle - \langle p_{yy}\rangle], \quad \sigma_{\rm dev} = \sqrt{\delta p^2 + \sigma^2}. \tag{14}$$

In the Appendix we present numerical results to show that while δp can be non-negligible at low ϕ and low Q, the difference between $\sigma_{\rm dev}$ and σ is always small for the range of parameters we consider.

Finally, we can define the granular temperature T_g in the usual way,

$$T_g \equiv \frac{1}{N}\sum_i m_i \langle |\delta \mathbf{v}_i|^2 \rangle. \tag{15}$$

We note that the kinetic part of the pressure $p^{\rm kin}$ is simply related to T_g by $p^{\rm kin} = nT_g$ with $n = N/L^2$ the density of particles.

It is convenient to work in terms of dimensionless quantities. We take the diameter of the small particles d_s, and the mass m_0, as our units of length and mass, respectively. We take τ_e as the unit of time. With these choices, stress in two dimensions is measured in units of m_0/τ_e^2, and so we can define a dimensionless pressure tensor $\mathbf{P} = (\tau_e^2/m_0)\mathbf{p}$.

Because we expect (and in the following section we confirm) that our system obeys Bagnoldian rheology, with $p,\sigma \sim \dot\gamma^2$ for sufficiently small $\dot\gamma$, we define the dimensionless Bagnold coefficients in terms of the components of $\mathbf{P}/(\dot\gamma\tau_e)^2$,

$$B_p \equiv \frac{p}{m_0\dot\gamma^2}, \quad B_\sigma \equiv \frac{\sigma}{m_0\dot\gamma^2}, \tag{16}$$

and similarly for the separate pieces, $B_p^{\rm el}$, $B_p^{\rm dis}$, $B_p^{\rm kin}$, etc. These dimensionless Bagnold coefficients are functions of only the dimensionless parameters ϕ, Q, and $\dot\gamma\tau_e$. As we will soon see, using τ_e as the unit of time will give Bagnold coefficients that become independent of Q at small Q for small $\dot\gamma\tau_e$ [14].

Note, the hard-core limit of infinitely stiff particles is usually considered as the limit $k_e \to \infty$, i.e., the interaction potential of Eq. (1) is so stiff that any particle overlaps are suppressed [28]. By Eq. (5) this implies $\tau_e \to 0$ for particles with finite mass. However, when expressed in the above dimensionless variables, we see that the hard-core limit is really the limit $\dot\gamma\tau_e \to 0$. Thus, even for soft-core particles with finite k_e, and so finite τ_e, we can reach the hard-core limit by taking a suitably small value of $\dot\gamma$ [16]. For sufficiently small $\dot\gamma\tau_e$ we expect the Bagnold coefficients B_p and B_σ to approach well-defined values that depend on ϕ and Q, but are independent of $\dot\gamma\tau_e$. These are the limiting hard-core values. How small $\dot\gamma\tau_e$ must be to reach this hard-core limit is not *a priori* known, it must be explicitly verified by simulations. Note also that this hard-core limit places no constraint on the value of Q. One should thus be careful to distinguish between the elasticity of particle interactions (i.e., stiffness of the particle core) governed by k_e or equivalently τ_e, and the elasticity of particle collisions (i.e., degree of energy conservation in a collision) governed by Q; the term elasticity has quite different meanings in these two different usages. The behavior of the hard-core Bagnold coefficients, as a function of ϕ and Q, will be the main concern of this work.

C. Simulation method

In our numerical simulations, we choose the diameter of the small particles to be $d_s = 1$, and the mass $m_0 = 1$, and take the unit of time $\tau_e = 1$ (which implies the elastic coupling $k_e = 1$). We integrate the equations of motion (4) using a modified velocity-Verlet algorithm with a Heun-like prestep to account for the velocity dependent acceleration. We use an integration time step given by the following heuristic formula that varies according to the value of Q, $\Delta t/\tau_e = \min\{0.5/Q, 0.1, 0.2Q\}$. The dependence of $\Delta t/\tau_e$ on Q is motivated by the following physical picture: at large Q, particles move quickly so small time steps are needed to resolve all collisions; at very small Q (large k_d), the dissipative force can become very large and too large a time step would cause particles to unphysically reverse direction rather than just slow down. We have tested that our heuristic formula satisfactorily gives results independent of further decreasing the time step [29].

We simulate for a range of strain rates from $\dot\gamma\tau_e = 10^{-3}$ down to 10^{-6}. For $\dot\gamma\tau_e = 10^{-5}$ (which corresponds to most of our presented results), we simulate out to a total strain $\gamma = \dot\gamma t$ of roughly $4 < \gamma < 100$, with the longest runs lying at intermediate values of $0.5 \lesssim Q \lesssim 10$. For $\dot\gamma\tau_e = 10^{-6}$ we simulate to a total strain of roughly $0.12 < \gamma < 10$, again with the longest runs at intermediate values of Q. In each case we exclude the initial 50% of the run in order to reach steady state, and then collect data for our averages from the remainder of the run. For each parameter point $(\phi, Q, \dot\gamma\tau_e)$ we average over at least five independent runs. Simulations at our largest $\dot\gamma$ are

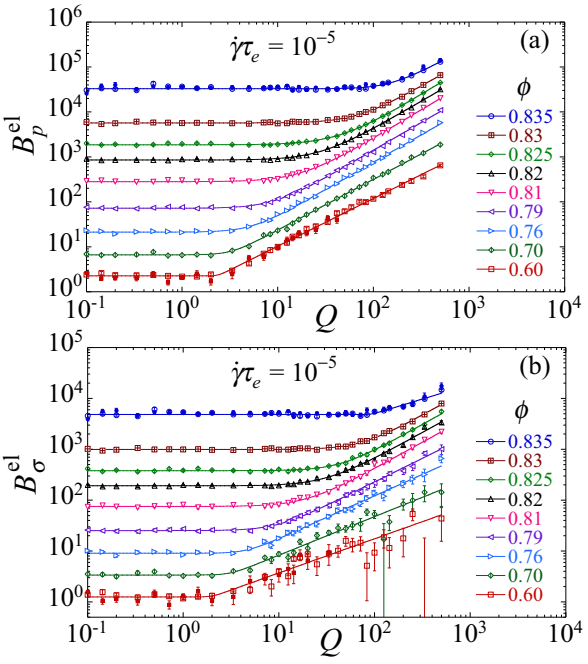

FIG. 1. The elastic part of the Bagnold coefficients for (a) pressure p and (b) shear stress σ vs collision elasticity parameter Q for different values of packing fraction ϕ, which goes from 0.835–0.60 as the curves go from top to bottom. Open symbols at all ϕ are for a shear strain rate $\dot\gamma\tau_e = 10^{-5}$; corresponding solid symbols at $\phi = 0.60$ and 0.835 are for $\dot\gamma\tau_e = 10^{-6}$. The absence of a dependence on $\dot\gamma\tau_e$ shows that results are in the hard-core limit.

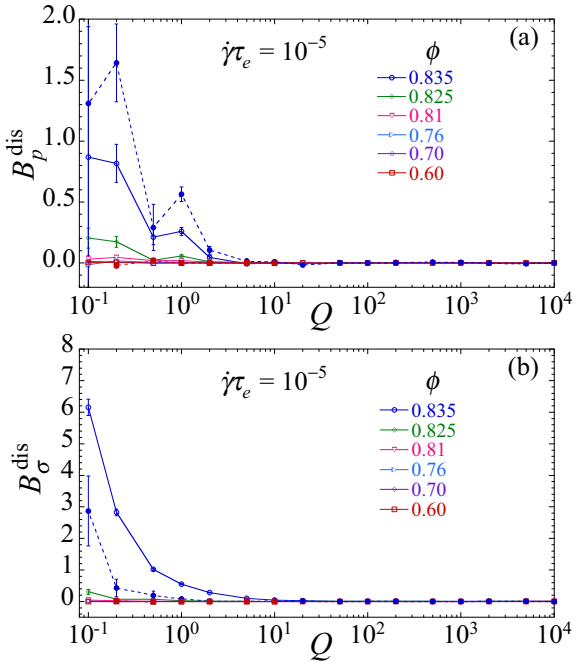

FIG. 2. The dissipative part of the Bagnold coefficients for (a) pressure p and (b) shear stress σ vs collision elasticity parameter Q for different values of packing fraction ϕ. Open symbols connected by solid lines at all ϕ are for a shear strain rate $\dot\gamma\tau_e = 10^{-5}$; corresponding solid symbols connected by dashed lines, at $\phi = 0.60$ and 0.835, are for $\dot\gamma\tau_e = 10^{-6}$.

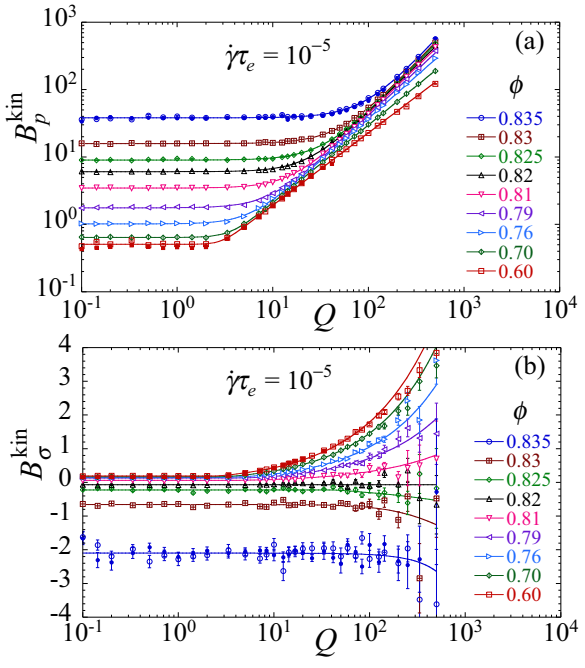

FIG. 3. The kinetic part of the Bagnold coefficients for (a) pressure p and (b) shear stress σ vs collision elasticity parameter Q for different values of packing fraction ϕ. In (a), ϕ decreases as the curves go from top to bottom; in (b) ϕ increases as the curves go from top to bottom. Open symbols at all ϕ are for a shear strain rate $\dot\gamma\tau_e = 10^{-5}$; corresponding solid symbols at $\phi = 0.60$ and 0.835 are for $\dot\gamma\tau_e = 10^{-6}$. The absence of a dependence on $\dot\gamma\tau_e$ shows that results are in the hard-core limit. Note the linear vertical scale in (b), which is necessary since $B_\sigma^{\rm kin}$ changes sign.

started from an initial random configuration at each (ϕ, Q); simulations at smaller $\dot\gamma$ start from a steady-state configuration sampled from the simulation at the next larger $\dot\gamma$, at the same value of (ϕ, Q).

III. RESULTS

In this section we describe our numerical results. We consider systems with a range of packing fractions from $\phi = 0.60$–0.835, and a range of Q from 0.1–500. Our range of Q corresponds to a coefficient of restitution for two small particles ranging from $e = 0$–0.9965 (for $Q < 0.564$, $e = 0$; for $Q = 2$, $e = 0.3970$; for $Q = 10$, $e = 0.8373$). In a previous work [5] we carried out a detailed critical scaling analysis of the jamming transition for the specific strongly inelastic case of $Q = 1$, determining the value of the packing fraction at jamming to be $\phi_J = 0.843\,35 \pm 0.000\,05$. Here we will present results to argue that the value of ϕ_J, as well as all other critical parameters at jamming, are independent of the particular value of Q.

Since our objective in the present work is to provide an understanding of the effect that varying Q has on the rheology, rather than a quantitative analysis of critical behavior at jamming, our investigations will avoid getting too close to ϕ_J; the closest we get to jamming will be $(\phi_J - 0.835)/\phi_J = 0.01$. This allows us to work with the relatively small system size of $N = 1024$ particles without incurring finite-size effects, and relatively large strain rates $\dot\gamma\tau_e \geqslant 10^{-6}$ that still put us in the hard-core limit; this can be compared to the values $N = 262\,144$ and $\dot\gamma\tau_e \geqslant 2 \times 10^{-8}$, which we used in Ref. [5].

A. Bagnold coefficients

In Figs. 1, 2, and 3 we present our results for the elastic, dissipative, and kinetic parts of the Bagnold coefficients for pressure p and shear stress σ, which we plot vs the elasticity parameter Q for different fixed values of the packing fraction ϕ. We show results for a shear strain rate $\dot\gamma\tau_e = 10^{-5}$, except for our smallest $\phi = 0.60$ and largest $\phi = 0.835$, where we show results for both $\dot\gamma\tau_e = 10^{-5}$ (open symbols) and $\dot\gamma\tau_e = 10^{-6}$ (solid symbols). The observed absence of any dependence of the results on $\dot\gamma\tau_e$ (except for $B_p^{\rm dis}$ and $B_\sigma^{\rm dis}$ at the smallest Q and largest ϕ, see more below) indicates that our results are at sufficiently small $\dot\gamma\tau_e$ to represent the hard-core limit. If we wished to explore closer to the jamming point $\phi_J = 0.843\,35$, it would be necessary to use smaller $\dot\gamma\tau_e$.

We consider first the dissipative parts $B_p^{\rm dis}$ and $B_\sigma^{\rm dis}$, shown in Fig. 2. At small Q, we have found that the dissipative part fluctuates rapidly as a function of time, and so it was the most difficult of the three parts to compute accurately; our results here tend to be from longer runs than used elsewhere. We see that both $B_p^{\rm dis}$ and $B_\sigma^{\rm dis}$ are essentially zero, except for the smallest Q at the very largest ϕ. For the largest $\phi = 0.835$ we see that $B_\sigma^{\rm dis}$ decreases substantially as the strain rate decreases from $\dot\gamma\tau_e = 10^{-5}$ (open circles) to 10^{-6} (solid circles). Considering other values of $\dot\gamma\tau_e$ (not shown here) our results suggest that $B_\sigma^{\rm dis} \sim \dot\gamma\tau_e$. In contrast, $B_p^{\rm dis}$ at $\phi = 0.835$ seems possibly to increase slightly as $\dot\gamma\tau_e$ decreases from 10^{-5} to 10^{-6}; however, the estimated errors here are large and

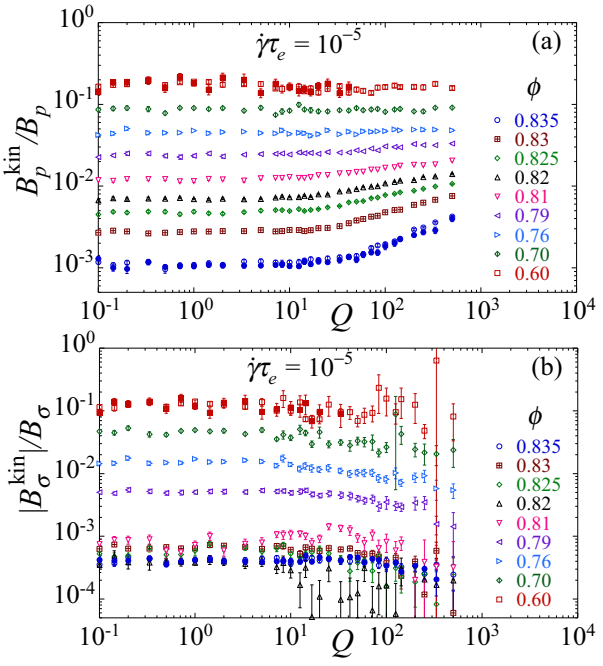

FIG. 4. Relative contribution of the kinetic part to the total Bagnold coefficient: (a) $B_p^{\rm kin}/B_p$ and (b) $|B_\sigma^{\rm kin}|/B_\sigma$ vs Q for different fixed packing fraction ϕ, which goes from 0.60–0.835 as the curves go from top to bottom. Open symbols at all ϕ are for a shear strain rate $\dot\gamma\tau_e = 10^{-5}$; solid symbols at $\phi = 0.60$ and 0.835 are for $\dot\gamma\tau_e = 10^{-6}$. Note, $B_p^{\rm kin}/B_p = nT_g/p$, with T_g the granular temperature.

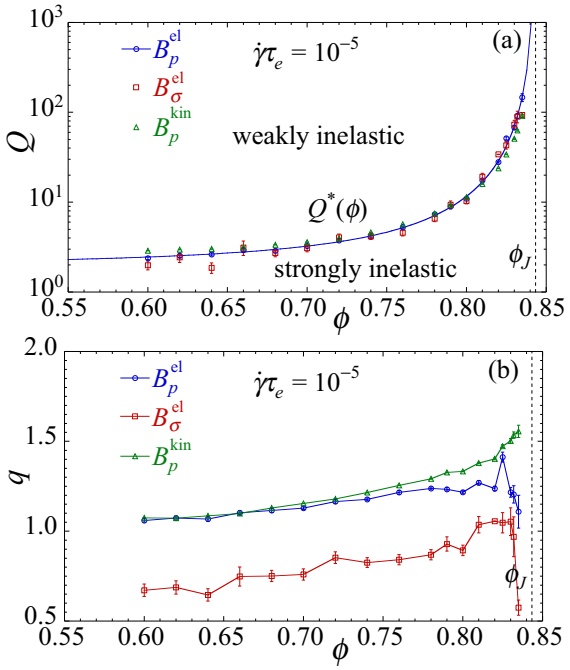

FIG. 5. (a) Phase diagram in the Q-ϕ plane, showing the crossover $Q^*(\phi)$ that separates the region of strongly inelastic behavior from weakly inelastic behavior. We show values for Q^* as determined independently from the Bagnold coefficients $B_p^{\rm el}$, $B_\sigma^{\rm el}$, and $B_p^{\rm kin}$ of Figs. 1 and 3(a); these are all found to agree. Solid line is a fit of Q^*, as obtained from $B_p^{\rm el}$, to the form $Q_0 + c(\phi_J - \phi)^{-x}$ with fixed $\phi_J = 0.843\,35$, and yields the value $x \approx 1.65$. (b) Exponents q that determine the large Q algebraic increase of the Bagnold coefficients $B_p^{\rm el}$, $B_\sigma^{\rm el}$, and $B_p^{\rm kin}$. In both panels the vertical dashed line locates the jamming transition at $\phi_J = 0.843\,35$. Results are from simulations with shear strain rate $\dot\gamma\tau_e = 10^{-5}$.

we cannot with confidence deduce a clear trend. In any case, comparing Fig. 2 with Fig. 1, we see that, for all values of ϕ and Q considered here, $B_p^{\rm dis}$ and $B_\sigma^{\rm dis}$ are completely negligible compared to $B_p^{\rm el}$ and $B_\sigma^{\rm el}$. We therefore henceforth ignore these terms and take $B_{p,\sigma} = B_{p,\sigma}^{\rm el} + B_{p,\sigma}^{\rm kin}$.

Considering next the kinetic parts $B_p^{\rm kin}$ and $B_\sigma^{\rm kin}$ in Fig. 3 we see that as ϕ increases, $B_p^{\rm kin}$ steadily increases, while $B_\sigma^{\rm kin}$ decreases, becoming negative as ϕ gets close to the jamming $\phi_J = 0.843\,35$. In Fig. 4 we plot the ratio $B_p^{\rm kin}/B_p$ and $|B_\sigma^{\rm kin}|/B_\sigma$ vs Q for different fixed ϕ. We see that the relative contribution of the kinetic part to the total Bagnold coefficient is largest at our smallest ϕ, where it is roughly 10%. But as ϕ increases, this relative contribution for p drops rapidly to 0.1–0.5% (depending on Q) at our largest $\phi = 0.835$; for σ it is in the range 0.05–0.1%. Thus the contribution of the kinetic part becomes negligibly small as the jamming point is approached, justifying the neglect of this term in our earlier scaling analysis [5] of the divergence of B_p and B_σ at jamming for small $Q = 1$.

We also note that, because of the relation between $p^{\rm kin}$ and the granular temperature T_g ($p^{\rm kin} = nT_g$), we have $B_p^{\rm kin}/B_p = nT_g/p$. If our athermally sheared system was behaving the same as an equilibrium system at thermal temperature $T = T_g$, we would expect that, in the hard-core limit, nT_g/p would be independent of the details of the dynamics and so a function solely of the packing fraction ϕ, independent of the parameter Q. The dependence of $B_p^{\rm kin}/B_p = nT_g/p$ on Q observed in Fig. 4(a), most notably at the larger values of ϕ, thus indicates the difference between shear induced fluctuations and thermal fluctuations.

Finally, we consider the elastic parts $B_p^{\rm el}$ and $B_\sigma^{\rm el}$ in Fig. 1. We see that at each ϕ there is a clear crossover value $Q^*(\phi)$, such that for $Q < Q^*$ the Bagnold coefficients are independent of Q, while for $Q > Q^*$ the Bagnold coefficients increase with Q algebraically. The value of $Q^*(\phi)$ increases as ϕ increases. The same behavior is also observed in the kinetic parts $B_p^{\rm kin}$ and $B_\sigma^{\rm kin}$. To determine the crossover values Q^* we fit our data to the phenomenological form $B = C[1 + (Q/Q^*)^s]^{q/s}$, which interpolates between the small and large Q behaviors. The exponent q gives the large Q algebraic behavior, while the parameter s determines the sharpness of the crossover at Q^*. The solid lines in Figs. 1 and 3 are the results of such fits.

In Fig. 5(a) we show the resulting phase diagram in the Q-ϕ plane, plotting the crossover $Q^*(\phi)$ that separates the region of strongly inelastic behavior ($Q < Q^*$) from weakly inelastic behavior ($Q > Q^*$). We show Q^* as determined from the above described fits, independently fitting to the data for $B_p^{\rm el}$, $B_\sigma^{\rm el}$, and $B_p^{\rm kin}$ shown previously in Figs. 1 and 3(a). We see that the values of Q^* obtained from these three quantities all agree nicely. We do not show results for $B_\sigma^{\rm kin}$ since, as may be seen in Fig. 3(b), the large scatter of the data at large Q, and the change in sign of $B_\sigma^{\rm kin}$ upon increasing ϕ, gives a poor fit

to our phenomenological form at the larger ϕ. In Fig. 5(b) we show the fitted values of the exponent q that give the large Q algebraic growth in the Bagnold coefficients. For the pressure parts, $B_p^{\rm el}$ and $B_p^{\rm kin}$, we see that q increases from roughly 1.1–1.5 as ϕ increases towards jamming; for the shear stress $B_\sigma^{\rm el}$, q is noticeable smaller, increasing from roughly 0.6–1.0. It is unclear if one should ascribe any fundamental significance to these particular values of q, of if they describe only empirical fits over the limited range of Q we have investigated.

B. Shear-driven jamming transition

We return to our results in Fig. 5(a). We denote the region $Q < Q^*$, where the Bagnold coefficients become independent of Q, as the strongly inelastic region, while $Q > Q^*$ is the weakly inelastic region. We discuss further some of the physical differences between these two regions in the next section.

An important feature of our result for $Q^*(\phi)$ is that Q^* appears to be diverging as ϕ increases towards the jamming ϕ_J. This would imply that a system at any fixed value of Q always crosses over from the weakly inelastic region into the strongly inelastic region, as ϕ increases above $\phi^*(Q)$, defined as the inverse of $Q^*(\phi)$. Since jamming thus always takes place in the strongly inelastic region, and since in the strongly inelastic region the values of B_p and B_σ are independent of the particular value of Q, the asymptotic divergence of these quantities upon jamming is the same for all Q. Hence the jamming packing fraction ϕ_J, and all jamming critical exponents, are the same for all Q and so equal to the values found in our earlier scaling analysis [5] carried out at the specific value of $Q = 1$.

Thus, the only effect that increasing Q has on the jamming transition is to decrease the region where strongly inelastic behavior (and its consequent critical scaling) holds. As Q diverges, and so collisions are perfectly elastic (energy conserving), this region shrinks to zero. So it is only for this case of perfectly elastic collisions that the jamming critical behavior may become different. The same conclusion was previously reached by OHL in Ref. [16].

To support this conclusion, we fit our data for Q^*, as obtained from $B_p^{\rm el}$, to the form $Q^*(\phi) = Q_0 + c(\phi_J - \phi)^{-x}$. The solid line in Fig. 5(a) is the result of such a fit keeping $\phi_J = 0.843\,35$ fixed at the value determined by Ref. [5], and yields the exponent of divergence $x \approx 1.65 \pm 0.02$ and $Q_0 = 1.89 \pm 0.06$. If we instead let ϕ_J be a free parameter, then the fit gives $\phi_J = 0.8425 \pm 0.0010$, $x = 1.59 \pm 0.07$, and $Q_0 = 1.8 \pm 0.1$, consistent with the previous result within the estimated errors. The fitted values do not change significantly if we shrink the window of the fitted data closer to ϕ_J.

To further illustrate the above point, in Fig. 6 we plot the total Bagnold coefficients B_p and B_σ vs ϕ, at different fixed values of Q. We see that the curves for different Q all are approaching a common curve, representing the strongly inelastic limit, as ϕ approaches ϕ_J. As ϕ decreases from ϕ_J, the curves peel off from this common curve at a $\phi^*(Q)$ that decreases as Q decreases. For the several smallest values of Q, the curves overlap for the entire range of ϕ shown.

As ϕ approaches close to the jamming ϕ_J, we expect to see a power-law divergence of the Bagnold coefficients, $B_{p,\sigma} \sim (\phi_J - \phi)^{-\beta}$. In our previous work of Ref. [5] at $Q = 1$ we

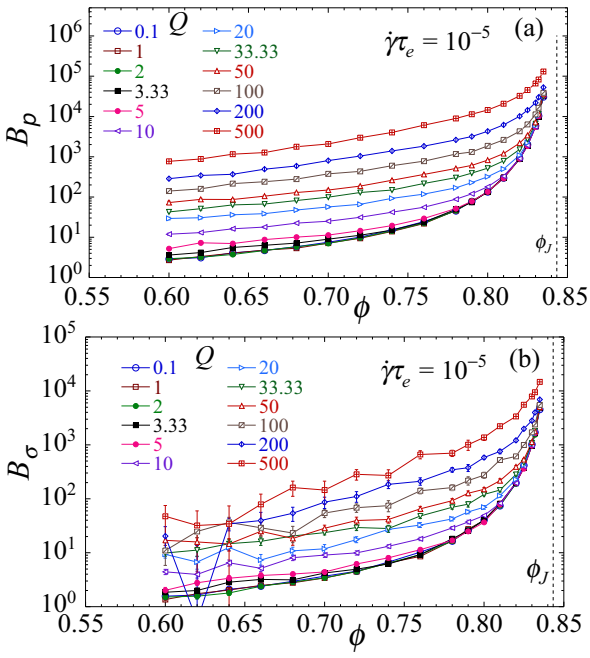

FIG. 6. Total Bagnold coefficients (a) B_p and (b) B_σ, for pressure p and shear stress σ respectively, vs packing fraction ϕ, for different fixed values of the collision elasticity parameter Q; Q increases from 0.1–500 as curves go from bottom to top. The vertical dashed line locates the jamming transition at $\phi_J = 0.843\,35$. Results are from simulations with shear strain rate $\dot\gamma\tau_e = 10^{-5}$.

argued that to see the true asymptotic divergence of B_p and B_σ at jamming one needs to get extremely close to ϕ_J and use very small strain rates $\dot\gamma$. Using a detailed critical scaling analysis, including leading corrections to scaling, we found $\beta = 5.0 \pm 0.4$ (see Ref. [5] for a discussion of how this value of β relates to those obtained in earlier numerical works). We further showed that if one fits a simple power law to the Bagnold coefficients over a wider range of ϕ and $\dot\gamma$, one finds only an effective exponent $\beta_{\rm eff} < \beta$, whose value depends on the window of data used in the fit (see Fig. 7 of Ref. [5]). In the present work, we do not get anywhere close enough to the jamming critical point to see the true exponent β. Nevertheless, we can still ask how the effective exponent $\beta_{\rm eff}$ will vary if one increases Q.

In Fig. 7 we replot our data for B_p and B_σ vs $\phi_J - \phi$, using $\phi_J = 0.843\,35$ from Ref. [5]. For small Q, where the data is in the strongly inelastic region for most of the values of ϕ, we find for our range of data $\beta_{\rm eff} \approx 3.3$ for B_p and 3.0 for B_σ. In contrast, for our largest $Q = 500$, where most of the data remains in the weakly inelastic region, we find $\beta_{\rm eff} \approx 1.3$ for B_p and 1.4 for B_σ. Thus, $\beta_{\rm eff}$ can decrease substantially as Q increases and collisions become increasingly elastic. If we further allowed ϕ_J to be a free fitting parameter, rather than fixing it to its known value as we have done here, it is possible that yet other values of $\beta_{\rm eff}$ may be obtained.

We can, in principle, include the effects of a varying Q within a critical scaling theory. If we assume that for $Q < Q_0$ the Bagnold coefficients are independent of Q for all ϕ, then for $\delta Q \equiv Q - Q_0 > 0$ we can regard δQ as a new scaling variable. Since $\delta Q > 0$ does not change the criticality of the

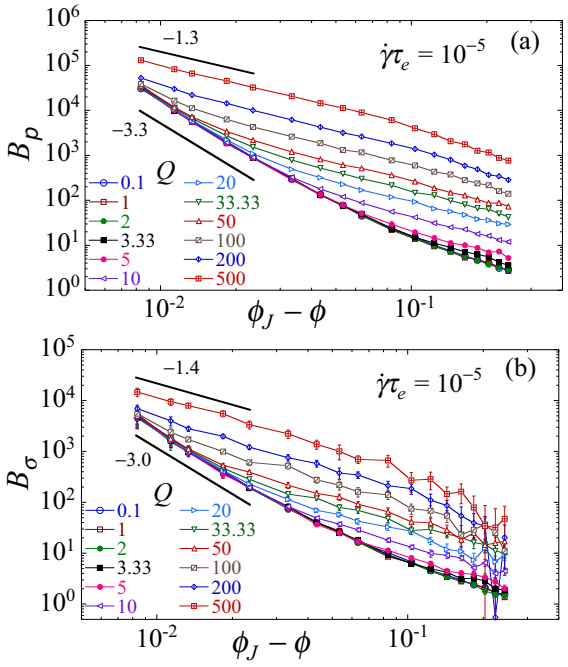

FIG. 7. Total Bagnold coefficients (a) B_p and (b) B_σ, for pressure p and shear stress σ, respectively, vs $\phi_J - \phi$, for different fixed values of the collision elasticity parameter Q; Q increases from 0.1–500 as curves go from bottom to top. We use $\phi_J = 0.843\,35$ from Ref. [5]. The bold straight lines, with slopes as indicated in the figure, denote the approximate power-law dependencies of our data closest to ϕ_J, for the smallest and largest values of Q (these are not the true power-law divergences asymptotically close to ϕ_J; see text). Results are from simulations with shear strain rate $\dot\gamma\tau_e = 10^{-5}$.

jamming transition, it is an irrelevant variable, and thus has a negative scaling exponent. We can then write the scaling equation [5] for B_p as,

$$B_p(\phi, Q, \dot\gamma) = b^{\beta/\nu} f(\delta\phi b^{1/\nu}, \dot\gamma b^z, \delta Q b^{-x/\nu}, w b^{-\omega}), \quad (17)$$

where b is an arbitrary length rescaling factor, $\delta\phi = \phi_J - \phi$, ν, and z are the correlation length and dynamic critical exponents respectively, and w is the leading irrelevant variable with exponent ω. If we then choose $b = \delta\phi^{-\nu}$, and consider the hard-core limit of $\dot\gamma \to 0$, the above becomes

$$B_p(\phi, Q) = \delta\phi^{-\beta} f(1, 0, \delta Q \delta\phi^x, w\delta\phi^{\omega\nu}). \quad (18)$$

If we were close enough to the jamming point so that the leading irrelevant variable $w\delta\phi^{\omega\nu}$ could be ignored, then plotting $B_p\delta\phi^\beta$ vs $\delta Q\delta\phi^x$ would yield a collapse of the curves for different δQ. However, our prior work in Ref. [5] has shown that the leading irrelevant variable cannot be ignored for the range of parameters considered here, so such a collapse is not possible for our data. Nevertheless, Eq. (18) still leads to the conclusion that the crossover from the strongly inelastic limit to the weakly inelastic limit is governed by the parameter $\delta Q\delta\phi^x$, and so takes place when $Q^* = Q_0 + c\delta\phi^{-x}$, consistent with our numerical results in Fig. 5(a).

Finally, we consider the macroscopic friction, $\mu \equiv \sigma/p$. Although the individual particles have frictionless contacts,

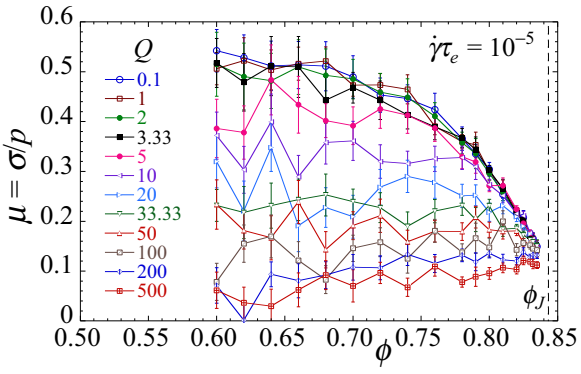

FIG. 8. Macroscopic friction $\mu \equiv \sigma/p$ vs ϕ for different fixed values of Q; Q increases from 0.1–500 as curves go from top to bottom. The vertical dashed line locates the jamming transition at $\phi_J = 0.843\,35$. Results are from simulations with shear strain rate $\dot\gamma\tau_e = 10^{-5}$.

the macroscopic friction remains finite. In Fig. 8 we plot μ vs ϕ for different fixed values of Q. We see that as ϕ approaches $\phi_J = 0.843\,35$, μ approaches a common value μ_J for all Q. In our prior work [5] we estimated $\mu_J \approx 0.093$. Although our results for μ are rather noisy, the trend in behavior as ϕ and Q are varied is clear. At the smallest Q, the curves for μ overlap for all ϕ, giving the limiting behavior of the strongly inelastic region, for which μ increases as ϕ decreases. For larger Q, μ follows this common curve until ϕ decreases below $\phi^*(Q)$, at which point $\mu(\phi, Q)$ falls below the strongly inelastic limit. For sufficiently large Q, μ even decreases as ϕ decreases, and can fall below the value of μ_J.

C. Strong vs weak inelastic regions

Having found the crossover $Q^*(\phi)$ between the strongly and weakly inelastic regions, we can ask what different physical signatures characterize the behavior in the different regions. One clear difference that we find concerns the angle of collision impact. To measure this, let us define,

$$\mathbf{r}_{ij} \equiv \mathbf{r}_i - \mathbf{r}_j, \quad \mathbf{v}_{ij} \equiv \mathbf{v}_i - \mathbf{v}_j, \quad (19)$$

as the position and velocity of particle i with respect to particle j. We then define the angle θ as the angle by which one must rotate $\mathbf{v}_{ij}$ to align it parallel with $\mathbf{r}_{ij}$ [30]. For two particles just initiating a contact, we must have $\hat{\mathbf{v}}_{ij} \cdot \hat{\mathbf{r}}_{ij} = \cos\theta < 0$, so that the particles are driven into each other, as illustrated in Fig. 9(a). In this case we must have $90^\circ < \theta < 270^\circ$. For two particles just breaking a contact, we must have $\hat{\mathbf{v}}_{ij} \cdot \hat{\mathbf{r}}_{ij} = \cos\theta > 0$, so that the particles are driven away from each other, as illustrated in Fig. 9(b). In this case we must have $-90^\circ < \theta < 90^\circ$.

Measuring the value of θ each time a contact is initiated and each time a contact is broken, we construct a histogram $\mathcal{P}(\theta)$, which combines both contact initiation and contact breaking events. In Fig. 10 we plot $\mathcal{P}(\theta)$ vs θ at several different values of Q, for the particular case of $\phi = 0.78$ for which $Q^* \approx 7.35$. For the weakly inelastic case of $Q = 500 \gg Q^*$ in Fig. 10(a), we see that $\mathcal{P}(\theta) \sim |\cos\theta|$, as would be expected if the collision impact parameter, $b = |\mathbf{r}_{ij} \times \hat{\mathbf{v}}_{ij}|$, is distributed uniformly on the interval $-d_{ij} < b < d_{ij}$. Thus, deep in the

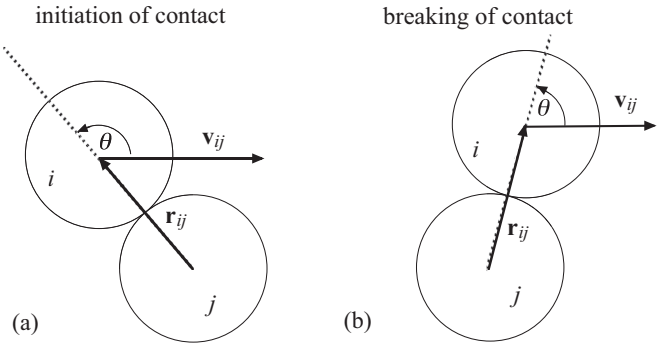

FIG. 9. Schematic of the collision of two particles i and j. (a) Initiation of contact, where $90^\circ < \theta < 270^\circ$, and (b) breaking of contact, where $-90^\circ < \theta < 90^\circ$. Here $\mathbf{r}_{ij} \equiv \mathbf{r}_i - \mathbf{r}_j$ and $\mathbf{v}_{ij} \equiv \mathbf{v}_i - \mathbf{v}_j$.

weakly inelastic region collisions occur at all angles, with a normal head-on collision at $\theta = 0$ being the most likely. In contrast, for the strongly inelastic case of $Q = 0.1 \ll Q^*$ in Fig. 10(f), we see that $\mathcal{P}(\theta)$ has sharp peaks at $\theta = \pm 90^\circ$, and $\mathcal{P}(\theta)$ is a minimum at $\theta = 0$. Thus, in the strongly inelastic region collisions involve mostly tangential relative motion between particles. Figures 10(b)–10(e) show $\mathcal{P}(\theta)$ at intermediate value of Q to illustrate how the distribution transforms between these two limits. We observe similar behavior at other values of ϕ. The reason for this behavior is simple. As Q gets small, the dissipative force of Eq. (3) damps out the relative normal motion of particles in contact, but does not effect the relative tangential motion.

We can get further insight into the different nature of collisions in the strong vs weak inelastic regions by considering the average time duration of a collision, $\tau_{\rm dur}$, and the average collision rate, $\nu_{\rm coll}$; $\tau_{\rm dur}$ is defined as the time from the initiation of a particular particle contact to the breaking of that contact, $\nu_{\rm coll}$ is defined as the average number of collisions per unit time divided by the number of particles. In Fig. 11(a) we plot $\tau_{\rm dur}/\tau_e$ vs Q, for the particular case of $\phi = 0.78$ and several different strain rates $\dot\gamma\tau_e$. We see that $\tau_{\rm dur}/\tau_e$ is essentially constant in the weakly inelastic region $Q > Q^*$; this constant value $\tau_{\rm dur}/\tau_e \approx 4$ is just slightly bigger than the large Q value for an isolated head-on collision between a small and big particle, which is 3.84 [6]. But as Q decreases into the strongly inelastic region, we see that $\tau_{\rm dur}/\tau_e$ rises over two orders of magnitude. For the strain rates considered here, we see that $\tau_{\rm dur}/\tau_e$ varies little with $\dot\gamma\tau_e$.

In Fig. 11(b) we plot the dimensionless $\nu_{\rm coll}/\dot\gamma$ vs Q for the same parameters as in Fig. 11(a), i.e., $\phi = 0.78$ and $\dot\gamma\tau_e = 10^{-4}, 10^{-5}$, and 10^{-6}. We see that in the weakly inlastic region, $Q > Q^*$, the curves for different $\dot\gamma\tau_e$ coincide, showing that $\nu_{\rm coll} \propto \dot\gamma$. In the strongly inelastic region, $Q < Q^*$, however, the curves separate, with the smaller strain rate curve lying above the higher strain rate curve; this shows that in the strongly inelastic region the collision rate $\nu_{\rm coll}$ grows more slowly than linearly with increasing $\dot\gamma$.

In Ref. [16] OHL give a relation between the average instantaneous particle contact number $\langle Z\rangle$ and the collision duration $\tau_{\rm dur}$ and rate $\nu_{\rm coll}$. Z is the number of contacts a given particle has with the other particles at any particular instant

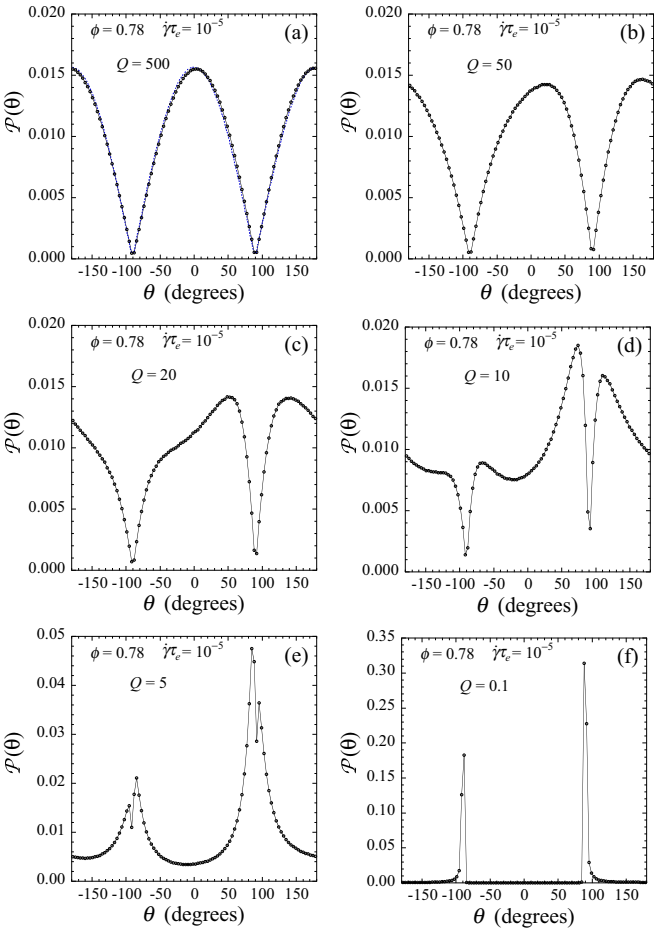

FIG. 10. Histograms $\mathcal{P}(\theta)$ vs collision angle θ, at initiation and breaking of particle contacts (see Fig. 9 for definition of θ), at $\phi = 0.78$. Results are shown for different values of the collision elasticity parameter Q. (a) $Q = 500$, (b) $Q = 50$, (c) $Q = 20$, (d) $Q = 10$, (e) $Q = 5$, and (f) $Q = 0.1$. The crossover $Q^* \approx 7.35$ at this value of ϕ. Dotted blue line in (a) is a fit to $\mathcal{P}(\theta) = C|\cos(\theta)|$. Results are for the shear strain rate $\dot\gamma\tau_e = 10^{-5}$.

in time. They argue that $\langle Z\rangle = 2\tau_{\rm dur}\nu_{\rm coll}$. Using our data in Fig. 11 we find excellent agreement with this prediction [31], as we show in Fig. 12. From this relation we can infer the behavior of $\langle Z\rangle$ as a function of the strain rate $\dot\gamma$. As argued by OHL [16], and reported by us recently [14], we find that in all regions below ϕ_J, $\langle Z\rangle \to 0$ as $\dot\gamma \to 0$. However, as we show now, the manner in which $\langle Z\rangle$ vanishes with decreasing $\dot\gamma$ differs in the two regions. In the weakly inelastic region, $Q > Q^*$, since from Fig. 11 we see that both $\tau_{\rm dur}/\tau_e$ and $\nu_{\rm coll}/\dot\gamma$ are independent of the strain rate $\dot\gamma\tau_e$, we conclude that $\langle Z\rangle \propto \dot\gamma\tau_e$ as $\dot\gamma \to 0$. But in the strongly inelastic region, $Q < Q^*$, we see that $\tau_{\rm dur}/\tau_e$ is roughly independent of $\dot\gamma\tau_e$ but $\nu_{\rm coll}/\dot\gamma$ is decreasing more slowly than linearly in the strain rate; hence we conclude that in the strongly inelastic region $\langle Z\rangle$ decreases more slowly than linearly with $\dot\gamma\tau_e$ as $\dot\gamma \to 0$.

We show this explicitly in Fig. 13. In Fig. 13(a) we show $\langle Z\rangle$ vs $\dot\gamma\tau_e$, for different values of Q, at the packing fraction $\phi = 0.78$ where $Q^* \approx 7.35$. We see that for large $Q \gtrsim Q^*$, $\langle Z\rangle$ decreases linearly with $\dot\gamma\tau_e$ as $\dot\gamma\tau_e \to 0$. However for $Q < Q^*$, $\langle Z\rangle$ decreases more slowly as $\dot\gamma\tau_e \to 0$. In Fig. 13(b)

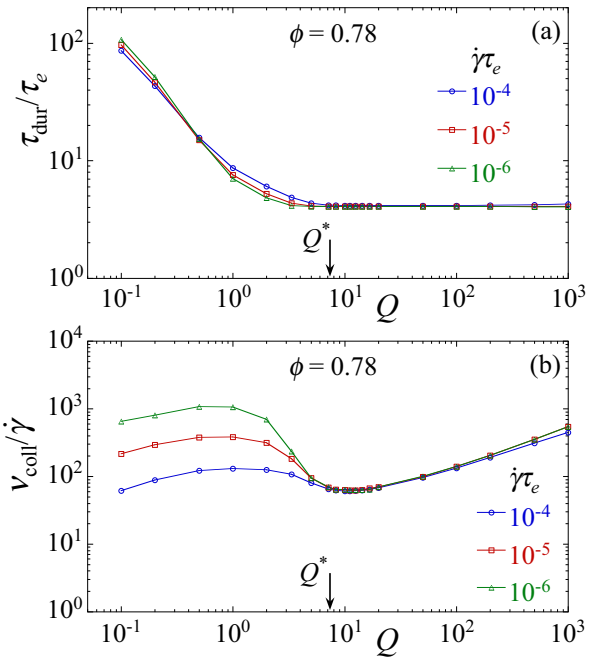

FIG. 11. (a) Average duration of collision τ_{dur}/τ_e, from time of initiation of contact to time of breaking of contact, vs collision elasticity parameter Q. (b) Ratio of average collision rate to strain rate, $\nu_{coll}/\dot\gamma$, vs Q. In both panels results are shown for packing fraction $\phi = 0.78$ and shear strain rates $\dot\gamma\tau_e = 10^{-4}$, 10^{-5}, and 10^{-6}. The crossover $Q^* \approx 7.35$, separating strongly from weakly inelastic regions, is denoted by the vertical arrow.

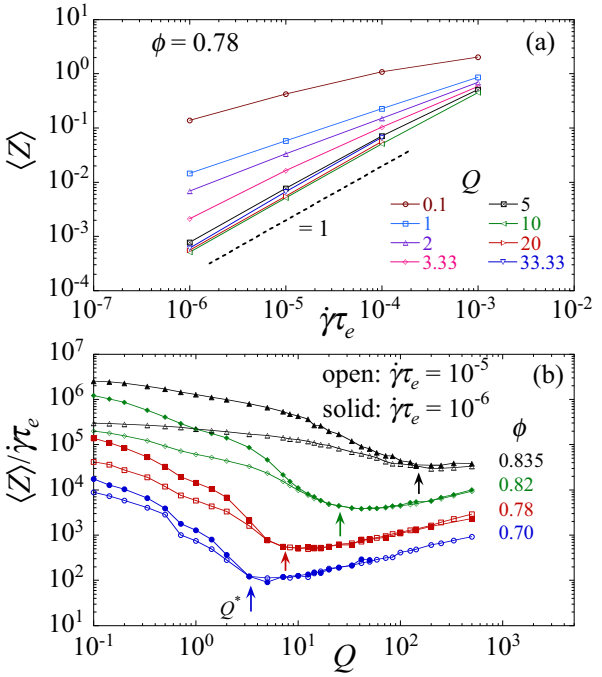

FIG. 13. (a) Average contact number $\langle Z\rangle$ vs strain rate $\dot\gamma\tau_e$ at $\phi = 0.78$, for different values of Q. The dashed line has slope of unity, indicating a linear relation at large Q. (b) $\langle Z\rangle/\dot\gamma\tau_e$ vs Q for $\dot\gamma\tau_e = 10^{-5}$ (open symbols) and 10^{-6} (solid symbols) at several different values of ϕ. Vertical arrows indicate the location of the crossover Q^* at each different ϕ.

we plot $\langle Z\rangle/\dot\gamma\tau_e$ vs Q for several different values of ϕ, at the two strain rates $\dot\gamma\tau_e = 10^{-5}$ and 10^{-6}. For $Q > Q^*$ we see that $\langle Z\rangle/\dot\gamma\tau_e$ is independent of $\dot\gamma\tau_e$, thus confirming that $\langle Z\rangle \propto \dot\gamma\tau_e$. For $Q < Q^*$, however, the curves separate, with the smaller $\dot\gamma\tau_e = 10^{-6}$ curve lying above the $\dot\gamma\tau_e = 10^{-5}$ curve; this indicates that $\langle Z\rangle$ is decreasing less rapidly than $\dot\gamma\tau_e$, as implied by the behavior of ν_{coll} in Fig. 11(b). We also see that $\langle Z\rangle$ is nonmonotonic in Q. This is a reflection of the increase in ν_{coll} with increasing Q at large Q, and the increase in τ_{dur} with decreasing Q at small Q.

One can ask what is the mechanism by which increasing the packing fraction ϕ results in an increase in the threshold Q^* below which normal relative motion is damped out, and the contact number $\langle Z\rangle$ decreases more slowly with $\dot\gamma\tau_e$.

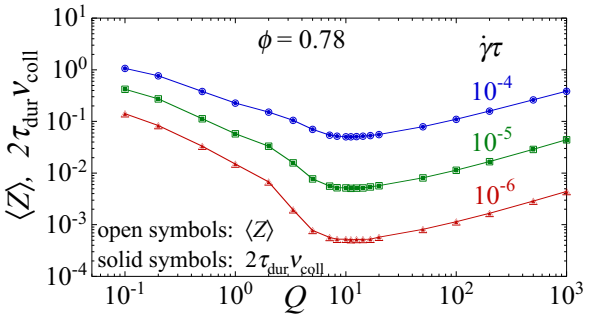

FIG. 12. Comparison of average particle contact number $\langle Z\rangle$ (open symbols) with $2\tau_{dur}\nu_{coll}$ (solid symbols) vs Q at packing fraction $\phi = 0.78$ for strain rates $\dot\gamma\tau_e = 10^{-4}$, 10^{-5}, and 10^{-6}.

Our preliminary investigation into this question suggests the following picture: for $Q > Q^*$ essentially all collisions are isolated binary collisions, where only two particles are in contact during any given collision; for $Q < Q^*$, however, we find that collisions become correlated, so that many collisions involve multiple particles in mutual contact. The number of such mutually contacted particles is found to grow as the density ϕ increases. Such an effect is presumably related to the decreasing free volume available to the particles as ϕ increases, and serves to renormalize the dissipative mechanism for damping relative normal motion, which leads to the increasing Q^* as ϕ increases. We leave further detailed exploration of this effect to future work.

As a final note, we have denoted the $Q < Q^*$ region, where the dissipative coupling k_d is large, as strongly inelastic (and $Q > Q^*$ as weakly inelastic) in analogy to the behavior of an isolated colliding pair. This analogy is supported by our results in Fig. 11(a), where we see that the collision duration time τ_{dur} is small and constant for $Q > Q^*$, but grows rapidly once Q decreases below Q^*. But this nomenclature is perhaps misleading in one respect. The rate of energy dissipation per volume in the system is $\Gamma = \sigma\dot\gamma = m_0 B_\sigma \dot\gamma^3$. From Fig. 1(b) or Fig. 6(b) we see that B_σ, and hence Γ, increases as Q increases into the weakly inelastic region. Thus, dissipation is smaller in the strongly inelastic region than it is in the weakly inelastic region, contrary to what one might naively expect. The reason for this behavior is given by Fig. 10. In the region $Q < Q^*$ the many particle steady state arranges itself so that collisions tend to involve only tangential relative motion. Since the

dissipative force of Eq. (3) depends only on the difference of the normal components of the particles' velocities, little energy is dissipated in such collisions. Our terminology "strongly inelastic" for $Q < Q^*$ thus refers specifically to the effect of a collision on the normal component of the relative motion of the colliding particles; tangential relative motion remains undamped at any Q.

D. Granular constitutive equations

In the previous sections we have discussed the dependence of quantities on the packing fraction ϕ, as appropriate for systems at constant volume. In the literature on hard granular materials, where pressure is often the regarded as the control parameter rather than volume, it is common to express quantities as a function of the inertial number I [21–25],

$$I \equiv \frac{\dot\gamma}{\sqrt{p/m_0}} = \frac{1}{\sqrt{B_p}}, \tag{20}$$

rather than the packing fraction ϕ. Since in the hard-core limit B_p is independent of $\dot\gamma$ and depends only on ϕ and Q, we have $I(\phi, Q)$, which can be inverted to write as $\phi(I, Q)$. We thus can regard I rather than ϕ as the control parameter; thus, in the hard-core limit, I is independent of the separate values of $\dot\gamma$ and p, and depends only on the combination as above in Eq. (20). Moreover, since in the hard-core limit B_σ is also a function of only ϕ and Q, we can substitute for ϕ in terms of I and write $B_\sigma(I, Q)$. We thus get the macroscopic friction $\mu = \sigma/p = B_\sigma/B_p$ as a function of I and Q. The two functions $\phi(I, Q)$ and $\mu(I, Q)$ are known as the constitutive equations. The jamming point corresponds to $I \to 0$ (i.e. $B_p \to \infty$).

For sufficiently small I close to jamming, it is observed empirically that the functions $\phi(I, Q)$ and $\mu(I, Q)$ can be written in the following form,

$$\phi(I) = \phi_J - c_\phi I^a, \quad \mu(I) = \mu_J + c_\mu I^b. \tag{21}$$

At the level of an empirical result, the coefficients c_ϕ and c_μ and exponents a and b might depend on Q; however we will argue below that as $I \to 0$, these parameters are in fact independent of Q.

It is often argued [22–24] that ϕ and μ are linear in the inertial number I, i.e., $a = b = 1$, for small I. However, the evidence for such linear behavior seems to be best found in systems in which there is a microscopic interparticle friction [21,32]. For frictionless particles, such as we consider here, Peyneau and Roux [25] considered a strongly inelastic system and found, from fits to a range $10^{-5} \leqslant I \leqslant 10^{-2}$, the exponents $a \approx b \approx 0.4$. Earlier work by da Cruz *et al.* [21] similarly found μ to be sublinear in I at small I for frictionless particles. Later work by Bouzid *et al.* [32] claimed $b = 1/2$, based on fits to a range $4 \times 10^{-4} \leqslant I \leqslant 10^{-1}$, for strongly inelastic frictionless particles.

In Ref. [5] we have shown that, in the asymptotic limit $I \to 0$, the form of the constitutive equations of Eq. (21) follows directly from the algebraic divergence of B_p and B_σ as $\phi \to \phi_J$, and the exponents a and b of the constitutive equations are related to the exponents β and $\omega\nu$ of Eq. (18) by,

$$a = 2/\beta, \quad b = 2\omega\nu/\beta = \omega\nu a. \tag{22}$$

In Ref. [5] we found $\omega\nu \approx 1$ and $\beta \approx 5$, thus suggesting $a = b = 2/\beta \approx 0.4$, in agreement with Peyneau and Roux [25]. Since we have argued in Sec. III B that the jamming transition always takes place within the strongly inelastic region $\phi > \phi^*(Q)$, where behavior is independent of the parameter Q, this then implies that the constitutive equations (21) likewise must be independent of Q, for sufficiently small I; hence we conclude that all the parameters that appear in Eq. (20) are independent of Q as $I \to 0$.

The above discussion was concerned with behavior asymptotically close to the jamming point $I \to 0$. It is interesting to now consider how the functions $\phi(I, Q)$ and $\mu(I, Q)$ behave as I increases out of the asymptotic small I region where Eq. (21) holds, and in particular when the system crosses into the weakly inelastic region $\phi < \phi^*(Q)$. In Fig. 14(a) we plot packing fraction ϕ vs inertial number I for various values of Q at a strain rate $\dot\gamma\tau_e = 10^{-5}$. From our results in Sec. III A we know this $\dot\gamma\tau_e$ is small enough to put one in the hard-core limit for the range of parameters considered here. On the linear-linear scale of Fig. 14(a), the data look qualitatively like the results of da Cruz *et al.* [21], and at moderate to high values of Q the data appear well approximated by a linear fit (the solid lines in the figure) over the wide range of I

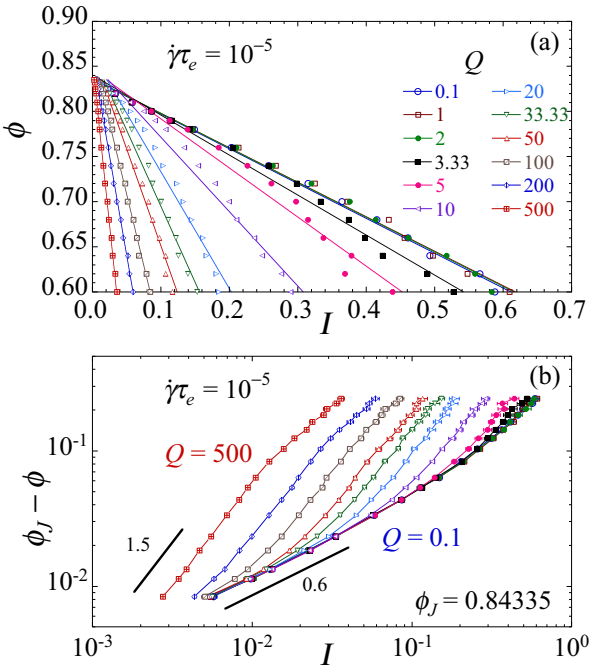

FIG. 14. (a) Packing fraction ϕ vs inertial number $I = \dot\gamma/\sqrt{p/m_0}$ for various values of Q. Straight lines are linear fits to the data. (b) Same as panel (a) but plotted as $\phi - \phi_J$ vs I on a log-log scale, where $\phi_J = 0.843\,35$ is taken from Ref. [5]. Solid lines correspond to power-law relations $\phi_J - \phi \propto I^{a_{\rm eff}}$ with $a_{\rm eff} = 1.5$ and 0.6 as shown. Symbols in panel (b) correspond to the legend in (a). Results are for a strain rate of $\dot\gamma\tau_e = 10^{-5}$.

shown. But if one looks closely at the data at the smallest I, approaching ϕ_J, one finds that these linear fits are really not doing very well. We see this explicitly in Fig. 14(b), where we plot $\phi_J - \phi$ vs I on a log-log scale; we use $\phi_J = 0.843\,35$ from our earlier work in Ref. [5]. We see that the slopes of the data at small I are not in general equal to unity, the value expected if we had the exponent $a = 1$. Figure 14(b) is just the analog of Fig. 7(a), and as found there, the curves at different Q all approach a common curve, characteristic of the strongly inelastic region $\phi > \phi^*(Q)$, as one gets sufficiently close to the jamming point $I \to 0$.

We may try to empirically fit our small I data in Fig. 14(b) to the form of Eq. (21). But since our data is not sufficiently close to the asymptotic $I \to 0$ limit, rather than finding the true asymptotic critical exponent a we will find for each Q only an effective power-law exponent $a_{\rm eff}$, which depends both on the value of Q and the range of I used in the fit. We see from Fig. 14(b) that, for our range of data, this $a_{\rm eff}$ ranges from about 0.6 at our smallest Q to 1.5 at our largest Q. That we find $a_{\rm eff} \approx 0.6$ at the smallest Q, rather than the value 0.4 expected by our work in Ref. [5] and as found by Peyneau and Roux [25], is simply because our small Q data, though already in the strongly inelastic region, is not at sufficiently small I to be in the true asymptotic jamming critical region. We thus see that, as with $\beta_{\rm eff}$ of Fig. 7(a), the value of $a_{\rm eff}$ for a finite range of I can be strongly affected by the value of Q.

Finally, we consider the macroscopic friction $\mu = \sigma/p$. In Fig. 15 we plot μ vs I for different Q at the strain rate $\dot\gamma\tau_e = 10^{-5}$. Again we see that curves for different Q approach a common curve characteristic of the strongly inelastic region $\phi > \phi^*(Q)$, as one gets close to jamming, $I \to 0$. But as I increases, the curves peel away from this common curve at an $I^*(Q)$ that decreases as Q increases. Similar results were found by Lois *et al.* [33]. Figure 15 is just the analog of Fig. 8, and again we see that for large Q, μ can decrease below the value μ_J at jamming as I increases. Fitting our data for the smallest $Q = 0.1$ in Fig. 15 to the form of Eq. (21), and taking $\mu_J = 0.093$ from Ref. [5], we find the exponent $b_{\rm eff} = 0.46 \pm 0.02$. This is larger than the expected $b \approx 0.4$ in the asymptotic limit $I \to 0$ [5,25], but close to the value $1/2$ found by Bouzid *et al.* [32]. As with $\beta_{\rm eff}$ and $a_{\rm eff}$, the value of $b_{\rm eff}$ depends on the range of I over which one fits, and may be influenced by the value of Q if part of the fitted data lies outside the strongly inelastic region.

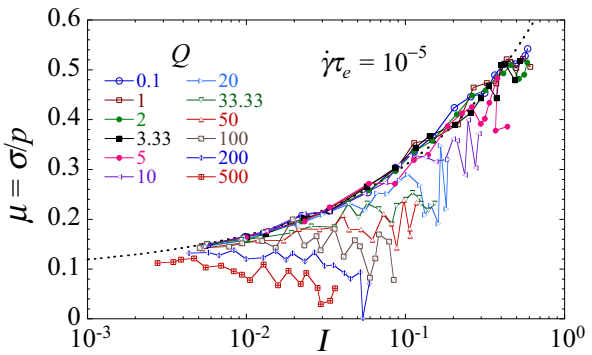

FIG. 15. Macroscopic friction $\mu = \sigma/p$ vs the inertial number $I = \dot\gamma/\sqrt{p/m_0}$ for various Q. Results are for a strain rate of $\dot\gamma\tau_e = 10^{-5}$. The dashed line is a fit to the form $\mu = \mu_J + c_\mu I^{b_{\rm eff}}$, with fixed $\mu_J = 0.093$ from Ref. [5], and gives the value $b_{\rm eff} \approx 0.46$.

IV. CONCLUSIONS

We have investigated the shear-driven Bagnold rheology of a simple model of athermal, soft-core, bidisperse, frictionless disks in two dimensions, as a function of the packing fraction ϕ and a parameter Q that controls the elasticity of collisions. We have shown that there is a $Q^*(\phi)$ that marks a sharp, but nonsingular, crossover from a region characteristic of strongly inelastic collisions ($Q < Q^*$), where normal relative motion of particles is strongly damped and the resulting relative motion is mostly tangential, to a region characteristic of weakly inelastic collisions ($Q > Q^*$). In the strongly inelastic region, transport coefficients are independent of the value of Q, while in the weakly inelastic region, transport coefficients grow algebraically with increasing Q. We have presented evidence that $Q^*(\phi)$ diverges as $\phi \to \phi_J$, the jamming transition, thus arguing that sufficiently close to ϕ_J one is always in the strongly inelastic region. As a consequence, the value of ϕ_J, and the critical exponents that characterize the divergence of the Bagnold transport coefficients, do not depend on the value of Q. However, we have also shown that effective exponents, obtained from fitting over windows of data wider than the true asymptotic region close to ϕ_J, can vary depending on the width of the data window and the value of Q.

We have shown that the weakly inelastic region is characterized by a collision rate $\nu_{\rm coll}$ and an average particle contact number $\langle Z\rangle$ that scale linearly with the strain rate $\dot\gamma$, while the duration time of collisions $\tau_{\rm dur}$ is largely independent of Q and $\dot\gamma$. Deep in the weakly inelastic region (i.e., nearly elastic), collisions are uniformly distributed over all impact parameters, and particles tend to bounce off each other after they collide.

In the strongly inelastic region, the collision rate $\nu_{\rm coll}$ and contact number $\langle Z\rangle$ still vanish as $\dot\gamma \to 0$, but they decrease more slowly than linearly in $\dot\gamma$. As Q decreases into the strongly inelastic region, the collision duration time $\tau_{\rm dur}$ grows rapidly, and collisions increasingly involve tangential relative motion between particles.

We believe that this crossover to tangential relative motion as Q decreases is a result of two different effects: (i) the damping out of particles' relative motion in the normal direction due to the dissipative force of Eq. (3), and (ii) the decreasing free volume available for particle motion as the packing fraction ϕ increases; this also greatly restricts relative motion in the normal direction, but less so for tangential relative motion. We believe it is this second effect that is responsible for the divergence of Q^* as $\phi \to \phi_J$.

We have also examined the macroscopic friction μ in our model and find that, while μ in the strongly inelastic region increases as ϕ decreases (or as inertial number I increases), once one enters the weakly inelastic region μ can decrease as ϕ further decreases (or as I further increase) and even fall below the value μ_J at jamming.

To summarize, we have shown that while the critical behavior asymptotically close to jamming is always characteristic of the strongly inelastic region, and so independent of the elasticity of collisions Q, the effect of collision elasticity can be clearly seen as one moves away from jamming.

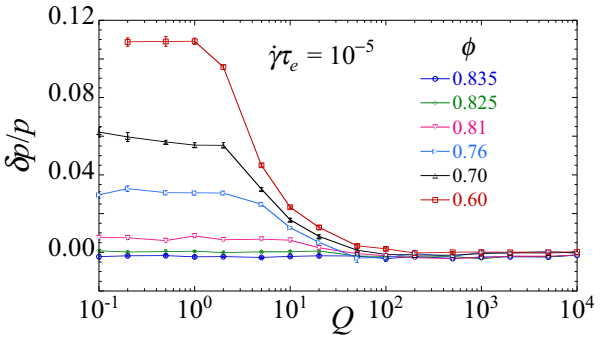

FIG. 16. The relative anisotropy in pressure, $\delta p/p$, vs Q for different values of packing fraction ϕ. The shear strain rate is $\dot\gamma\tau_e = 10^{-5}$ and the system has $N = 1024$ particles. The value of ϕ increases as the curves go from top to bottom.

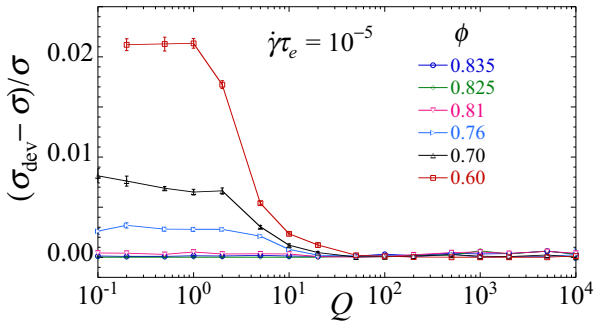

FIG. 17. The relative difference between deviatoric shear stress and off-diagonal stress, $(\sigma_{\rm dev} - \sigma)/\sigma$, vs Q for different values of packing fraction ϕ. The shear strain rate is $\dot\gamma\tau_e = 10^{-5}$ and the system has $N = 1024$ particles. The value of ϕ increases as the curves go from top to bottom.

ACKNOWLEDGMENTS

This work was supported by National Science Foundation Grant No. DMR-1205800, the Swedish Research Council Grant No. 2010-3725, and the European Research Council under the European Unions Seventh Framework Programme (FP7/2007-2013), ERC Grant Agreement No. 306845. Simulations were performed on resources provided by the Swedish National Infrastructure for Computing (SNIC) at PDC and HPC2N. We wish to thank H. Hayakawa and M. Otsuki for helpful discussions.

APPENDIX

In this Appendix we provide numerical results for the anisotropy in pressure,

$$\delta p \equiv \tfrac{1}{2}[\langle p_{xx}\rangle - \langle p_{yy}\rangle], \tag{A1}$$

and the deviatoric stress,

$$\sigma_{\rm dev} \equiv \sqrt{\delta p^2 + \sigma^2}, \tag{A2}$$

where $\sigma = -\langle p_{xy}\rangle$. The eigenvalues of the stress tensor are just $p \pm \sigma_{\rm dev}$, so a finite δp results in a slight shift in the orientation of the principle axes of the stress tensor from those of the strain tensor.

In Fig. 16 we plot $\delta p/p$ vs Q for several different packing fractions ϕ. Our results are for a system with $N = 1024$ particles and a shear strain rate of $\dot\gamma\tau_e = 10^{-5}$. We see that for all ϕ, $\delta p/p$ is very small at high Q. However, for small $Q \lesssim 10$, $\delta p/p$ can be of the order $5 - 12\%$ at the smaller values of ϕ. We find that the contribution to δp from the dissipative part of the pressure tensor is always negligible, while the elastic part contributes roughly twice as much as the kinetic part at low ϕ; as ϕ decreases, the relative contribution of the kinetic part tends to increase.

In Fig. 17 we show the corresponding results for $(\sigma_{\rm dev} - \sigma)/\sigma$. Here we see that this quantity is fairly small everywhere, reaching its largest value of $\sim 2\%$ for the smallest $\phi = 0.60$ at small $Q \lesssim 1$. We can understand why $(\sigma_{\rm dev} - \sigma)/\sigma$ is small by writing,

$$\frac{\sigma_{\rm dev} - \sigma}{\sigma} = \sqrt{\left[\left(\frac{\delta p/p}{\sigma/p}\right)^2 + 1\right]} - 1. \tag{A3}$$

Comparing Fig. 16 with Fig. 8, we see that where $\delta p/p$ is largest, $\sigma/p = \mu$ is also largest, with the result that the first factor under the square root is always small.

[1] C. S. O'Hern, L. E. Silbert, A. J. Liu, and S. R. Nagel, Phys. Rev. E **68**, 011306 (2003).
[2] A. J. Liu and S. R. Nagel, Annu. Rev. Condens. Matter Phys. **1**, 347 (2010).
[3] P. Olsson and S. Teitel, Phys. Rev. Lett. **99**, 178001 (2007).
[4] P. Olsson and S. Teitel, Phys. Rev. E **83**, 030302(R) (2011).
[5] D. Vågberg, P. Olsson, and S. Teitel, Phys. Rev. E **93**, 052902 (2016).
[6] J. Schafer, S. Dippel, and D. E. Wolf, J. Phys. I (France) **6**, 5 (1996).
[7] G. Lois, A. Lemaître, and J. M. Carlson, Phys. Rev. E **72**, 051303 (2005).
[8] M. Otsuki and H. Hayakawa, Prog. Theor. Phys. **121**, 647 (2009).
[9] M. Otsuki and H. Hayakawa, Phys. Rev. E **80**, 011308 (2009).
[10] T. Hatano, J. Phys. Soc. Jpn. **77**, 123002 (2008).
[11] T. Hatano, Prog. Theor. Phys. Suppl. **184**, 143 (2010).
[12] T. Hatano, J. Phys.: Conf. Ser. **319**, 012011 (2011).
[13] M. Otsuki and H. Hayakawa, Prog. Theor. Phys. Suppl. **195**, 129 (2012).
[14] D. Vågberg, P. Olsson, and S. Teitel, Phys. Rev. Lett. **112**, 208303 (2014).
[15] R. A. Bagnold, Proc. R. Soc. London A **225**, 49 (1954).
[16] M. Otsuki, H. Hayakawa, and S. Luding, Prog. Theor. Phys. **184**, 110 (2010).
[17] S. Luding, Nonlinearity **22**, R101 (2009).
[18] R. Garcia-Rojo, S. Luding, and J. J. Brey, Phys. Rev. E **74**, 061305 (2006).

[19] E. Khain, Europhys. Lett. **87**, 14001 (2009).
[20] For a recent analytical calculation, see K. Suzuki and H. Hayakawa, Phys. Rev. Lett. **115**, 098001 (2015).
[21] F. da Cruz, S. Emam, M. Prochnow, J.-N. Roux, and F. Chevoir, Phys. Rev. E **72**, 021309 (2005).
[22] O. Pouliquen, C. Cassar, P. Jop, Y. Forterre, and M. Nicolas, J. Stat. Mech. (2006) P07020.
[23] Y. Forterre and O. Pouliquen, Annu. Rev. Fluid Mech. **40**, 1 (2008).
[24] A. Lemaître, J.-N. Roux, and F. Chevois, Rheol. Acta **48**, 925 (2009).
[25] P.-E. Peyneau and J.-N. Roux, Phys. Rev. E **78**, 011307 (2008).
[26] Note that in Ref. [5] we erroneously stated that the unit of mass was taken as $m_s = 1$. In fact, the masses in that work are taken as described here, with the unit of mass $m_0 = 1$. Furthermore, τ_e and τ_d in that work are also defined with respect to m_0, as described here, and not with respect to m_s as was erroneously stated.
[27] D. J. Evans and G. P. Morriss, *Statistical Mechanics of Non-equilibrium Liquids* (Academic Press, London, 1990).
[28] C. S. Campbell, J. Fluid Mech. **465**, 261 (2002).
[29] If one is only exploring states already close to the steady state, then it is no longer necessary to employ the condition $\Delta t/\tau_e \leqslant 0.5/Q$ at large Q, since near the steady state the velocity scale is set by the strain rate $\dot{\gamma}$ and so does not get uncontrollably large. However, this condition is useful to include when starting in states that are far from the steady state, and this is what we used in practice.
[30] Our present convention for the angle θ gives the opposite sign from how we defined it in the Supplemental Material to Ref. [14]. Note also that in that work, the histogram $\mathcal{P}(\theta)$ was computed over all contacts at all times, whereas in the present work the histogram is computed over only contacts at the instant of initiation and the instant of breaking.
[31] In Ref. [16] the authors use an analytic expression for $\tau_{\rm dur}$ appropriate for the head-on collision of two particles, rather than compute $\tau_{\rm dur}$ directly. We believe this may be the reason they see close, but not perfect, agreement with $\langle Z \rangle = 2\tau_{\rm dur}\nu_{\rm coll}$ in their Fig. 8(b).
[32] M. Bouzid, M. Trulsson, P. Claudin, E. Clément, and B. Andreotti, Phys. Rev. Lett. **111**, 238301 (2013).
[33] See the inset to Fig. 5(a) in Ref. [23]; the data shown there comes from the work of Lois *et al.* in Ref. [7].